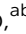





Cite this: DOI: 10.1039/d3ta01729j

# Modelling electro-chemically induced stresses in all-solid-state batteries: screening electrolyte and cathode materials in composite cathodes†

Robert Mücke, \*<sup>ab</sup> Najma Yaqoob, <sup>abc</sup> Martin Finsterbusch, <sup>ab</sup> Fadi Al-Jaljoui, <sup>abd</sup> Payam Kaghazchi, <sup>abc</sup> Dina Fattakhova-Rohlfing <sup>abe</sup> and Olivier Guillon <sup>abd</sup>

All-solid-state lithium batteries (ASSBs) are gaining significant attention worldwide as one of the most promising alternatives to lithium-ion batteries due to their superior safety and potentially higher energy density. However, one of the main problems of known ASSBs remains rapid capacity degradation, which needs to be addressed before their large-scale market introduction. One important degradation mechanism is the mechanical fatigue of the cathode layer due to the volume change of the cathode active material (CAM) during cycling. Quasi-zero-strain CAMs such as  $\text{Li}_x\text{Ni}_{0.3}\text{Co}_{0.6}\text{Mn}_{0.1}\text{O}_2$  (NCM361) and  $\text{Li}_x\text{Ni}_{0.2}\text{Co}_{0.7}\text{Mn}_{0.1}\text{O}_2$  (NCM 271) could solve this problem, but their use in ASSBs has not been investigated yet. We theoretically investigate the suitability of these CAMs in composite cathodes with various solid electrolytes such as poly(ethylene oxide) (PEO),  $\text{Li}_3\text{PS}_4$  (LPS),  $\text{Li}_{1.3}\text{Al}_{0.3}\text{Ti}_{1.7}(\text{PO}_4)_3$  (LATP) and  $\text{Li}_7\text{La}_3\text{Zr}_2\text{O}_{12}$  (LLZO) with respect to the mechanical stresses occurring at microscopic grain level and compare them with  $\text{Li}_x\text{Ni}_{0.9}\text{Co}_{0.05}\text{Mn}_{0.05}\text{O}_2$  (NCM955) and  $\text{LiCoO}_2$  (LCO). Although the quasi-zero-strain materials develop stresses in the GPa range during cycling, they still exhibit the lowest stresses of all the CAMs studied and could be of particular interest when using stiff electrolytes such as LATP or LLZO. High-capacity NCMs such as NCM955 exhibit a large volume change and should preferably be used together with electrolytes with bulk modulus less than 25 GPa such as PEO and LPS. While for soft electrolytes such as PEO and LPS the difference between the lattice strains along the different axes of the active material determines the stresses, for stiff electrolytes such as LATP and LLZO the total volume change is more important. Finally, a method is introduced to determine the stresses quickly from the free macroscopic strain mismatch without stress simulations.

Received 22nd March 2023

Accepted 8th July 2023

DOI: 10.1039/d3ta01729j

rsc.li/materials-a

## Introduction

All-solid-state batteries (ASSB) are gaining a lot of attention worldwide as one of the most promising alternatives to lithium-ion batteries (LIBs) due to an expected improvement in cell properties in terms of safety, energy density and operating temperature range. Various solid electrolytes are currently being considered for ASSB fabrication, mostly of the oxide,

sulfide, halide or polymer type, each with its advantages and disadvantages. Although important breakthroughs have been reached in various systems, such as an exceptional ionic conductivity of sulfide electrolytes or high current densities with Li metal anodes obtained with oxide electrolytes, the performance of liquid-free ASSB still lags behind that of LIBs. In particular, the fabrication of cathodes with high energy density and high cycling stability remains one of the most pressing problems of known ASSBs, which needs to be solved before large-scale market introduction.

To achieve competitive energy and power densities, the cathode layers should contain a large amount of high energy density cathode active material distributed in the solid electrolyte, similar to the three-dimensional composite cathode architecture in LIBs. Layered oxides of the quasi-ternary phase diagram  $\text{LiCoO}_2\text{-LiNiO}_2\text{-LiMnO}_2$  ( $\text{Li}_x\text{Ni}_{1-y-z}\text{Co}_y\text{Mn}_z\text{O}_2$ , NCM) are state-of-the-art cathode active materials to achieve high energy densities and enable high currents. However, all these oxides suffer from degradation during cycling, and the fracture of cathode particles due to non-negligible volume changes

\*Forschungszentrum Jülich GmbH, Institute of Energy and Climate Research, Materials Synthesis and Processing (IEK-1), Jülich, 52425, Germany. E-mail: r.muecke@fz-juelich.de

<sup>b</sup>Jülich Aachen Research Alliance: JARA-Energy, Jülich, 52425, Germany

<sup>c</sup>MESA+ Institute for Nanotechnology, University of Twente, P. O. Box 217, Enschede, 7500AE, The Netherlands

<sup>d</sup>Department of Ceramics and Refractory Materials, Institute of Mineral Engineering, RWTH Aachen University, 52064, Aachen, Germany

<sup>e</sup>Faculty of Engineering and Center for Nanointegration Duisburg-Essen, Universität Duisburg-Essen, Lotharstr. 1, 47057, Duisburg, Germany

† Electronic supplementary information (ESI) available. See DOI: <https://doi.org/10.1039/d3ta01729j>



during lithiation and delithiation plays a crucial role.<sup>1–10</sup> Nickel-rich NCMs such as  $\text{Li}_x\text{Ni}_{0.9}\text{Co}_{0.05}\text{Mn}_{0.05}\text{O}_2$  (NCM955) are very attractive cathode active materials because they yield very good energy density and avoid cobalt for economic, security, and ethical reasons. However, this comes with a drawback of a rather high chemical lattice strain of up-to  $-4\%$ . Attempts have been undertaken to develop quasi-zero-strain NCM materials with minimised volume change, such as  $\text{Li}_x\text{Ni}_{0.3}\text{Co}_{0.6}\text{Mn}_{0.1}\text{O}_2$  (NCM361) and  $\text{Li}_x\text{Ni}_{0.2}\text{Co}_{0.7}\text{Mn}_{0.1}\text{O}_2$  (NCM271),<sup>11</sup> which have a capacity of  $\sim 160 \text{ mA h g}_{\text{NCM}}^{-1}$  at 4.3 V and  $210 \text{ mA h g}_{\text{NCM}}^{-1}$  at 4.6 V. However, significant lattice strains also occur in these materials during lithiation and delithiation ( $\epsilon_a = -1.1\%$  and  $\epsilon_c = +1.3\%$  for NCM361). It should be noted that it is not the final stress but the maximum accompanying stress that governs the degree of mechanical degradation. The maximum stresses occur at about  $x = 0.5$  and decrease again at  $x = 0.2$  (compare Fig. 4 of ref. 11).

Mechanical degradation is exacerbated when solid electrolytes are used instead of liquid electrolytes in the composite cathodes, and is considered by many researchers to be the main reason for the capacity loss of ASSBs during cycling.<sup>12</sup> Due to the rigid structure of solid electrolytes, their ability to absorb and distribute stresses deteriorates, resulting in large local stresses throughout the entire cathode architecture and mechanical failure of various interfaces. The stress development is affected by the anisotropy of the cathode active material lattice and the particle distribution, as well as by the type of solid electrolyte.<sup>13–16</sup> Different solid electrolytes in composite cathodes exhibit a strong variation of mechanical properties and thus significantly affect the overall stress state.  $\text{Li}_7\text{La}_3\text{Zr}_2\text{O}_{12}$  (LLZO) is an intensively investigated oxide ceramic with good electrochemical stability against various CAMs,<sup>17,18</sup> and is so far the only ceramic electrolyte that is (electro-)chemically stable toward Li metal anodes.<sup>19</sup> It exhibits a rather high (isotropic) mechanical stiffness of approximately 145 GPa. The NASICON-type solid electrolyte  $\text{Li}_{1.3}\text{Al}_{0.3}\text{Ti}_{1.7}(\text{PO}_4)_3$  (LATP) exhibits a comparable stiffness, but with pronounced rhombohedral anisotropy. In addition to the oxides, the sulphides form another main group of ceramic electrolytes, among which the thio-phosphates have the highest conductivity.<sup>20</sup> They exhibit a rather low stiffness (20–30 GPa)<sup>21</sup> and offer good mechanical ductility. We analysed  $\text{Li}_3\text{PS}_4$  (LPS) from this group as an example to compare it with the other electrolytes. Furthermore, polymers are another very important group of solid electrolytes for all-solid-state battery. One candidate is poly(ethylene oxide) (PEO) with extremely low stiffness (0.1 GPa) and high strain tolerance, which has already been used in composite LCO/PEO cathodes.<sup>22</sup>

The models for predicting stresses are important for the development of ASSBs as they allow the screening of various material composition and electrode architectures without extensive experimental studies. In our previous work, we developed a theoretical approach to study the anisotropic stress distributions in a LCO/LLZO composite cathode.<sup>13</sup> Using computer-generated microstructures, we further showed that for low  $C$  rates (equilibrium Li concentration) the grain size has no significant effect on the mechanical stresses whereas the

LCO : LLZO ratio exhibited a significant linear effect, keeping the difference in the stress levels of the two phases constant, and the porosity showed a non-linear effect.<sup>23</sup> In the present work, we use an experimental and four computer-generated microstructures to investigate other prospective cathode active materials and solid electrolytes to explore their potential to reduce the mechanical stresses in the microstructure. We theoretically investigate the suitability of quasi-zero-strain cathode active materials such as NCM361 and NCM271 in composite cathodes with important solid electrolytes such as PEO, LPS, LATP and LLZO with respect to the mechanical stresses occurring at grain level and compare them with NCM955 and LCO. To study only the effect of material parameters, the same microstructure applicable for all cases was used to model the mechanical behaviour of all materials based on the experimental microstructure of LCO–LLZO cathodes, the results were confirmed by three more computer-generated microstructures with different CAM content and porosity and one reference computer-generated structure. Unknown anisotropic elastic stiffness matrices for some of cathode materials during charge/discharge ( $\text{Li}_{0.5}\text{NCM271}$ ,  $\text{Li}_{0.5}\text{NCM955}$ ,  $\text{Li}_{0.1}\text{NCM955}$ ,  $\text{Li}_{0.5}\text{CoO}_2$ ) were calculated using density functional theory (DFT). The material parameters that lead to the stresses were analysed to find the origin of the stresses and to find a common relationship between all stresses. Based on this we present an approach which allows the stress determination without complex simulations which can be useful in future material screenings.

## Results and discussion

First we focus on the experimental microstructure, at the end we compare some results with the computer-generated structures. Without any electrolyte material in the cathode, the pure LCO and NCM networks develop mechanical stresses during delithiation because of their anisotropic electro-chemical strains and the random orientation of the connecting grains (Fig. 1a–d). The different crystallographic orientations lead to a mismatch of chemical strains of adjacent grains along the same macroscopic direction. It should be noted that compressive stresses of the observed order will not cause failure in oxide materials as under compression the fracture strength is extremely high. Tensile stresses are more serious. However, in the absence of stress concentrators (typically large pores of tens or hundreds of microns, cracks, *etc.*) at the microscopic level the tensile strength of single crystals and whiskers in the micrometre range is also very high (in the GPa range, typically at least one order of magnitude larger than the tensile strength measured macroscopically for a polycrystalline ceramic). Out of this reason, well-sintered composite cathodes with low porosity prepared *e.g.* by field assisted sintering<sup>24</sup> might be more stress tolerant than traditionally sintered electrodes that show a residual porosity and cracks after cycling.<sup>10</sup>

The corresponding stress histograms indicate the most narrow stress distribution with the smallest stresses for NCM271, followed by NCM361 and LCO (Fig. 2a–d).  $\text{Li}_{0.5}\text{NCM955}$  showed the broadest distribution with



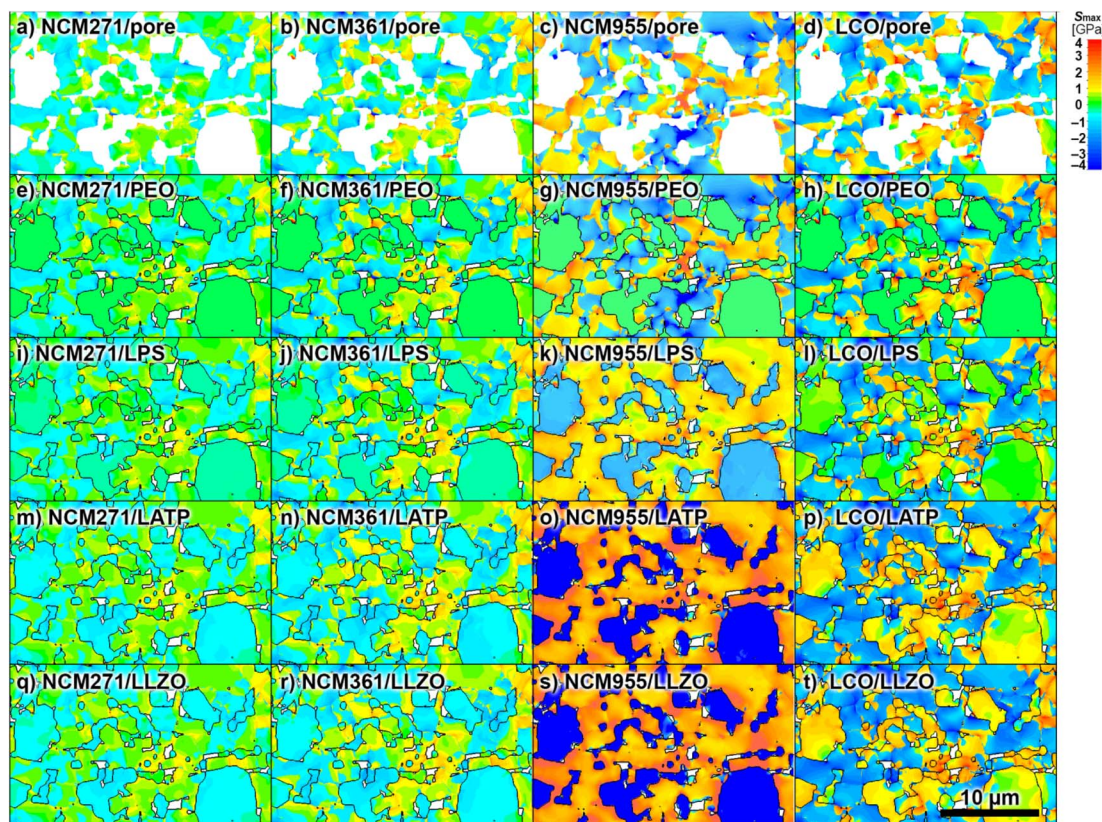


Fig. 1 Stress maps (principle stress with maximum absolute value) of a cross section of the delithiated porous/composite cathode with different cathode active materials and electrolyte materials for the configuration with the max. stresses: Li = 0.1 for (k), (o) and (s) and Li = 0.5 for all others. (a–d) Pure cathode active materials, (e–h) with PEO, (i–l) with LPS, (m–p) with LATP, (q–t) with LLZO as electrolyte material.

microscopic tensile stresses well above 1.5 GPa due to its high stiffness and strain anisotropy (the stress distribution of  $\text{Li}_{0.1}\text{NCM955}$  is shown in Fig. S1†). As the cathodes are free-standing and can expand freely macroscopically, high chemical strains alone do not lead to high stresses in pure cathode active polycrystalline materials, but the strain difference between the two different chemical lattice strains, namely  $\varepsilon_{c,\text{ch}} - \varepsilon_{a,\text{ch}}$ , control the stress state together with the materials' stiffness. Plotting the width of the stress distribution vs. the mere strain difference of the different materials a common trend to higher stress values for higher strain differences is observed (Fig. 2u).  $\text{Li}_{0.1}\text{NCM955}$  shows the smallest stress values because of the small difference in the strain components  $\varepsilon_{c,\text{ch}} - \varepsilon_{a,\text{ch}}$ . However, in order to obtain this high degree of delithiation,  $\text{Li}_{0.5}\text{NCM955}$  with a lower Li content has to be reached beforehand which is accompanied with the highest stresses because of the large difference in the strain components. The points ( $\Delta_{\text{ch}}$ ) still scatter significantly. This scattering becomes slightly smaller considering the absolute value of the developing stresses  $\Sigma_{\Delta} = |\varepsilon_{c,\text{ch}} - \varepsilon_{a,\text{ch}}| / (c_{11}^{-1} + c_{33}^{-1})$  according to an iso-strain model of two adjacent grains with a perpendicular orientation leading to maximum strain difference. The remaining scattering shows that the real situation with arbitrary grain boundary angles and non-uniform stress states is more complex.

In the following, the stress results of composite cathodes with various electrolyte materials in ascending order of their stiffness are presented. PEO exhibits an extremely small Young's modulus (approx. 3 orders of magnitude lower than the cathode active material); in consequence it can compensate almost all stresses by deformation when acting as electrolyte in a composite cathode (Fig. 2e–h), the stresses inside PEO are practically zero. Furthermore, no change in the stress state in the cathode active material was observed with or without PEO (Fig. 1a–h, compare Fig. 2e–h with Fig. 2a–d).

Using LPS as electrolyte material in the composite cathode introduces a slight shift of the stress distribution inside the cathode active materials (Fig. 2i–l). This shift is smallest for NCM271 and NCM361, followed by LCO, and very significant for NCM955 (0.49 GPa). The stress distributions of LCO/LPS are shifted in the opposite direction than the distributions of the other three combinations as LCO is the only material that expands during delithiation. Also the shape of the distributions changed: the sharp maxima at zero stress were reduced and widened as the cathode active material directly in contact with the electrolyte material cannot expand freely anymore but is significantly constrained. The width of the distributions remained unchanged except for the case of NCM955. In this case  $\text{Li}_{0.1}\text{NCM955}$  with a smaller stress distribution width was considered as it introduces the largest stresses in the electrolyte



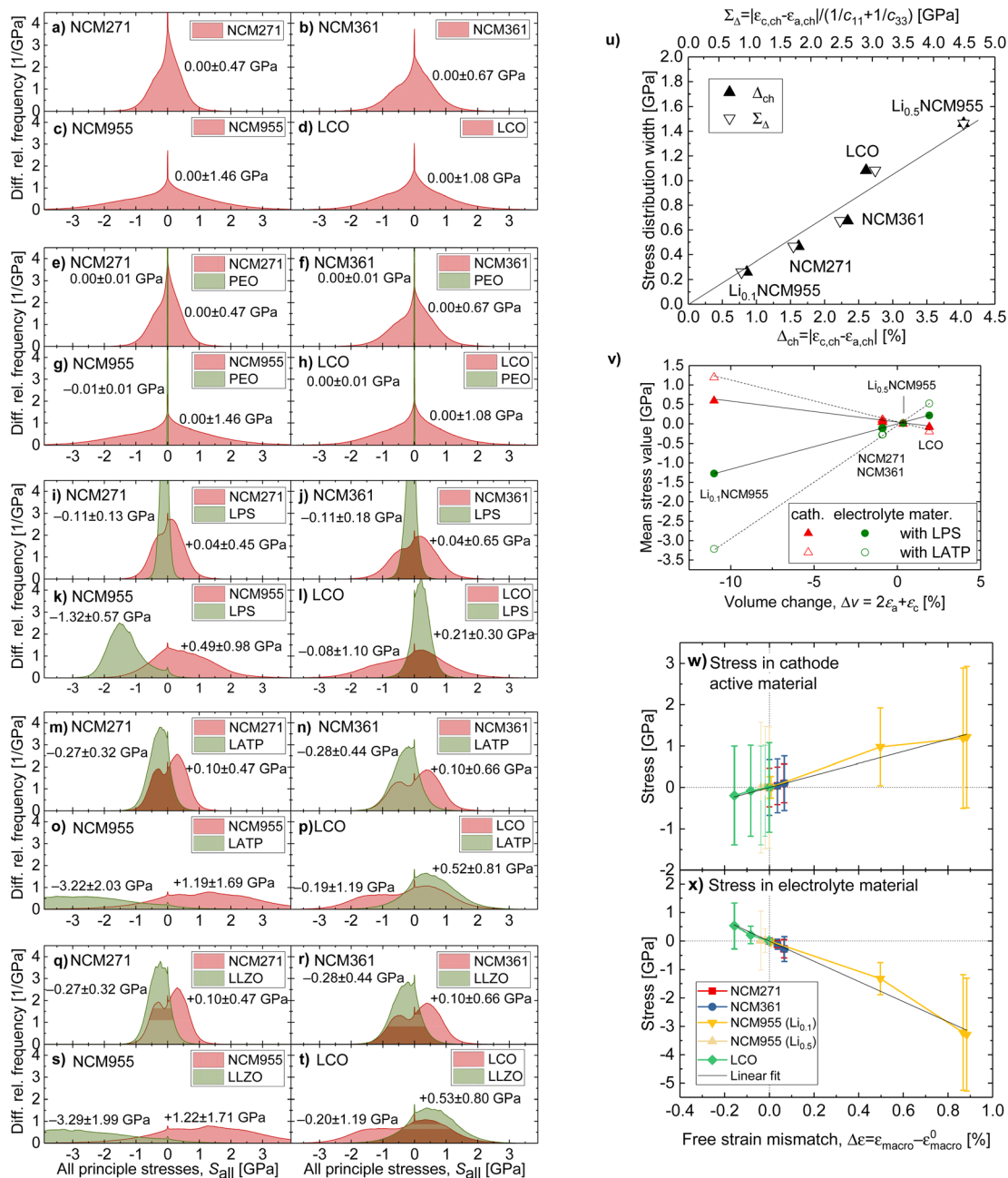


Fig. 2 (a–d) Histograms of all principal stresses inside different pure polycrystalline cathode active materials with random crystallographic grain orientation, (e–h) with PEO electrolyte material, (i–l) with LPS electrolyte material, (m–p) with LTP as electrolyte material, (q–t) with LLZO as electrolyte material. (c and g)  $\text{Li}_{0.5}\text{NCM955}$ , (k, o and s)  $\text{Li}_{0.1}\text{NCM955}$ . The mean value and the width (standard deviation) of distributions are given. (u) Width of the stress distribution of (a)–(d) as a function of the electro-chemical crystallographic strain difference ( $\Delta\epsilon_{\text{ch}}$ ) and the corresponding stresses ( $\Sigma_{\Delta}$ ). (v) Mean stress values of the cathode active and electrolyte material of the composite cathode as a function of the volume change for different electrolytes (LLZO would behave very similar to LTP). (w and x) Stress in cathode active material (w) and electrolyte material (x) of composite cathodes as a function of the free strain mismatch for various cathode active materials. The error bars indicate the width (standard deviation) of the stress distribution.

(the stress distribution of  $\text{Li}_{0.5}\text{NCM955}$  is given in Fig. S1c†). NCM955 shows a significant general increase of the stress levels (Fig. 1g and k) which is caused by the very high absolute values of the chemical strains of NCM955 against LPS with non-negligible stiffness. Typically, cell stacks with LPS based cells are compressed *e.g.* with 250 MPa during operation. The final

stress results with compression are given in Fig. S2,† they do not differ significantly from the calculations without compression.

Whereas only the difference of the anisotropic strains component mattered for the pure cathode active materials the value of the total volume change becomes more important once a more or less rigid electrolyte phase is introduced in the



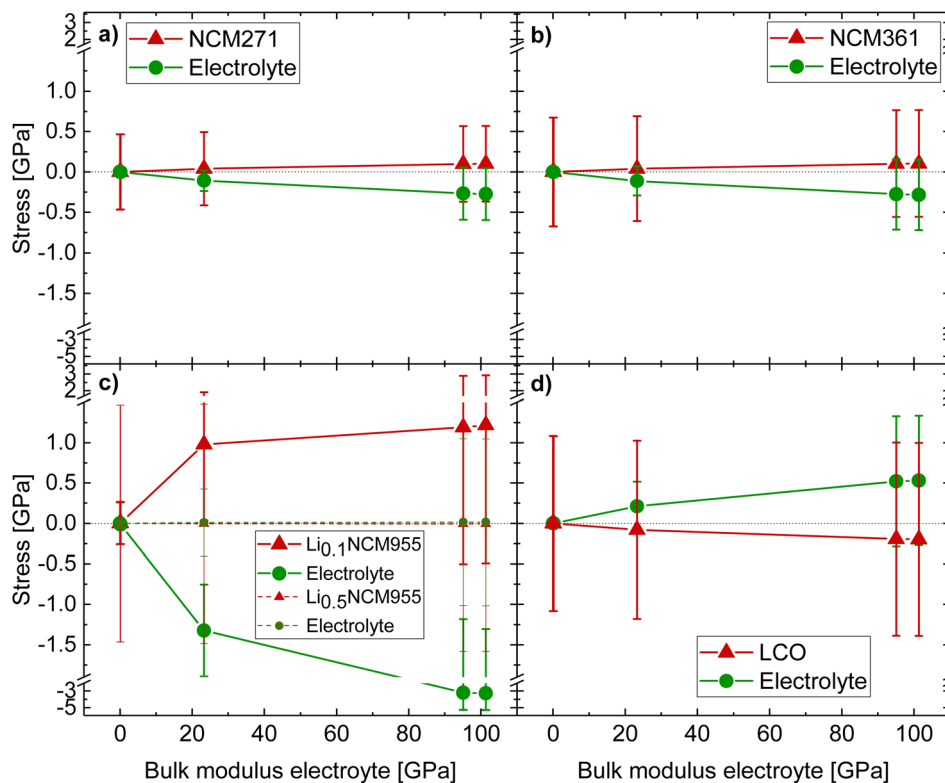


Fig. 3 Average principal stresses inside composite cathodes with different cathode active materials (a–d) as a function of the bulk modulus of the electrolyte material. The error bars indicate the width (standard deviation) of the stress distribution.

Table 1 Slopes of the stress-free strain difference curves of (Fig. 2w and x) and of more modelled microstructures (Fig. S4–S7, ESI). Exp./mod. = experimental/modelled microstructure. The volume ratio between CAM : electrolyte material (ELC) and the porosity (%) are given

Exp./Mod.	CAM : ELC	Por., %	$\sigma_{\text{CAM}}/\Delta\varepsilon$ , GPa/%	$\sigma_{\text{ELC}}/\Delta\varepsilon$ , GPa/%
Exp.	2 : 1	7	+1.5 ± 0.2	−3.5 ± 0.4
Mod.	2 : 1	7	+1.3 ± 0.2	−2.8 ± 0.3
Mod.	1 : 1	7	+1.2 ± 0.2	−1.2 ± 0.2
Mod.	1 : 2	7	+1.5 ± 0.3	−0.7 ± 0.2
Mod.	2 : 1	20	+0.8 ± 0.1	−1.8 ± 0.2

composite cathode. The mean principle stress value ( $\sigma_{\text{mean}}$ ) inside the cathode material is proportional to the relative volume change ( $\Delta v$ ) of the cathode active material (Fig. 2v, more details in Fig. S3†). The absolute value of the proportionality factor ( $\sigma_{\text{mean}}/\Delta v$ ) increases non-linearly with increasing electrolyte stiffness (Fig. S3c†). Due to the stiffness of LPS the stresses inside the electrolyte material are not negligible anymore, but also grow with the chemical strains of the cathode material and its stiffness. The highest value is reached in combination with  $\text{Li}_{0.1}\text{NCM955}$ .

With LTP as electrolyte material, the shift of the stress distributions of the cathode active materials becomes more significant as for LPS as electrolyte material whereas the order of the cathode active materials from high to low shift levels remains the same (Fig. 2m–p). The maximum value, 1.19 GPa, was reached with NCM955/LTP. For LCO and in particular for

NCM955 the width of the distribution widened significantly due to higher overall stress levels (Fig. 2o and p).

When LLZO is used as electrolyte material, the stress states (Fig. 2q–t) are almost identical to the stress states with LTP as the average stiffness is similar. The stiffness anisotropy of LTP does not change the effective principle stresses.

In order to get an overview about the mean stress values, all values together with their distribution width are plotted as a function of the bulk modulus of the electrolyte in Fig. 3. This modulus governs the stiffness of the rigid electrolyte framework against which the cathode active material has to expand or shrink. The absolute mean stresses inside the cathode active material and the electrolyte material of the composite cathode first grow quickly with increasing bulk modulus of the electrolyte material. This increase slows down for bulk moduli bigger than 24 GPa. Therefore a soft electrolyte with a bulk modulus smaller than approx. 25 GPa is preferable in particular for large strain cathode active materials. The quasi-zero-strain NCM materials (NCM271, NCM361) develop the smallest stresses considering also the width of the distribution. The magnitude of the stress level inside the active material is comparable to that for LCO. The stresses inside the electrolyte material are much smaller in composite cathodes with NCM271 and NCM361 compared to cathodes with LCO.

A common relationship for the stress values of all combinations analysed is found when plotting the strain vs. the difference of the average macroscopic strain with and without



electrolyte material (Fig. 2w and x). The expansion of the pure cathode active material,  $\epsilon_{\text{macro}}^0$ , can be calculated and the expansion of the composite cathode,  $\epsilon_{\text{macro}}$ , can be measured. Then, the mean values of the stresses can be obtained easily. Table S1† shows that for not too low CAM content (CAM : electrolyte material  $\geq 1 : 1$ ) the known mean lattice strains  $(2\epsilon_a + \epsilon_b)/3$  can be used for  $\epsilon_{\text{macro}}^0$ . The slope of a linear fit is  $(+1.5 \pm 0.1)$  GPa/% for the stress inside the cathode active material, and  $(-3.5 \pm 0.4)$  GPa/% for the stress inside the electrolyte material. Once the dependency of these slopes on the microstructure is found, a very general model for the stresses inside composite cathodes can be given without the necessity of stress simulations. Table 1 summarises the slopes also for four modelled microstructures with different cathode active material contents and porosity. The difference in both slopes ( $\sigma_{\text{CAM}}/\Delta\epsilon$  and  $\sigma_{\text{ELC}}/\Delta\epsilon$ ) between the experimental and the same modelled microstructure is mainly that the point of  $\text{Li}_{0.1}\text{NCM955/LPS}$  deviates in the opposite direction of the proportionality fit line. However, considering the margin of error the slopes are in agreement. Whereas the CAM content did not change the slope  $\sigma_{\text{CAM}}/\Delta\epsilon$  it significantly affects  $\sigma_{\text{ELC}}/\Delta\epsilon$ . The porosity changes both slopes.

## Conclusions

There are four reasons for the mechanical stresses in all solid composite cathodes occurring during electrochemical cycling: (1) The difference of anisotropic lattice expansion in pure cathode active materials. This introduces already stresses in pure active materials with sintered randomly oriented polycrystals. (2) With a rigid and stiff electrolyte the overall volume change of cathode active material becomes more important, the mean values of the stresses are proportional to the volume change. (3) In particular the stiffness (bulk modulus) of the electrolyte material. It determines the proportionality factor between mean stress and volume change. (4) The stiffness of the active material (they differ not much, however).

Applied to the materials screened it follows: the quasi-zero-strain NCM materials (NCM271 and NCM361) still develop stresses in the GPa range on the grain level over the course of delithiation, but exhibit the smallest stresses among all materials investigated. This might be of particular interest when stiff electrolytes like LATP or LLZO are used. However, NCM271 and NCM361 still consist of a remarkable amount of cobalt (60% and 70% of that of LCO, respectively) which might reduce their attractiveness for large scale application. For high-strain NCM955 cathode material a bulk modulus of the electrolyte material of 25 GPa or less is preferable (LPS or PEO electrolyte). Alternatively, a hybrid-electrolyte approach could be of interest, combining low and high bulk modulus materials to reduce the overall induced stresses.

Finally, all stresses depend proportionally on the free strain mismatch. This will also be the case for constrained composite cathodes layers *e.g.* on a thick separator. This measure can be used to predict the stresses easily. An initial general dependency of the corresponding proportionality factors on the microstructural parameters has been presented.

## Experimental and simulation methods

### Microstructure

The three dimensional microstructure of a sintered LLZO/LCO composite cathode was acquired by FIB-SEM and cropped to  $26.5 \times 16.5 \times 16.5 \mu\text{m}$  ( $530 \times 330 \times 330$  voxels) with a voxel size of 50 nm (Fig. 4a). The LLZO:LCO volume ratio was 2:1. Details can be found elsewhere.<sup>13</sup> The same microstructure was used for different electrolyte or cathode active materials during the screening, in order to obtain the impact of the materials only. The microstructure used for modelling the mechanical behaviour in our work is very typical for composite cathodes fabricated from powders slurries by conventional methods. This microstructure was observed experimentally for the ceramic LCO-LLZO composite cathodes fabricated by various methods, *e.g.*, screen-printed cathodes<sup>25</sup> or tape-cast free-standing cathodes.<sup>26,27</sup> Similar to LCO, NCM is also a hexagonal layered oxide with comparable size and shape of the commercial powders, so replacing LCO with NCM powders should not significantly affect the microstructure of composite cathodes. This was confirmed by a very similar microstructure of screen-printed NCM-LLZO cathodes, which have comparable relative density and porosity to the LCO-LZO cathodes.<sup>28</sup> If PEO is infiltrated in a sintered porous cathode active network, then it will resemble the sintered LLZO phase of this study. The grains were segmented using the watershed method (GrainFind module of GeoDict, Math2Market GmbH, Kaiserslautern, Germany) and the crystallographic orientation was chosen randomly by appropriate Euler angles ( $\phi$ ,  $\theta$ ,  $\psi$ ) to obtain a uniform distribution of the coordinate axes on the unit sphere (Fig. 4b). All calculations have been repeated on four computer-generated microstructures taken from ref. 23 with varying CAM content

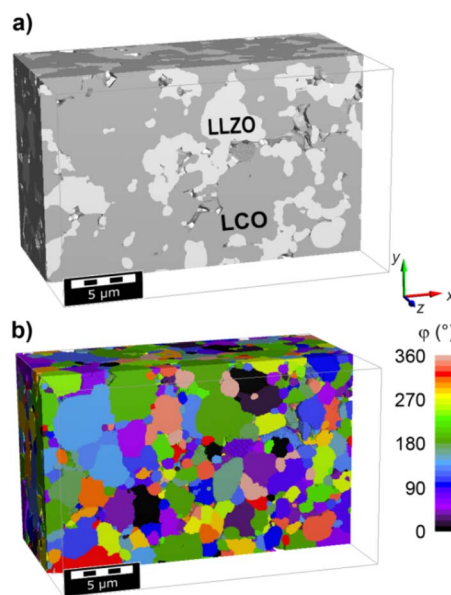


Fig. 4 (a) Slice of the reconstructed 3D microstructure, (b) distribution of the Euler angle  $\phi$  of the randomly oriented grains after segmentation.



and porosity in order to find the microstructure dependent slopes similar that of Fig. 2w and x for different microstructure parameters summarised in Table 1.

### Calculation of the strains and stiffness matrix of cathode active materials

Spin-polarized DFT calculations were performed using the projector augmented wave (PAW) potential method<sup>29</sup> implemented in the Vienna *Ab Initio* Simulation Package (VASP) code.<sup>30</sup> Generalized gradient approximation (GGA) within the scheme of Perdew–Burke–Ernzerhof (PBE)<sup>31</sup> was chosen as the exchange–correlation functional. To perform electrostatic energy analysis as well as DFT calculations we modelled  $\text{Li}_x\text{Ni}_{0.2}\text{Co}_{0.7}\text{Mn}_{0.1}\text{O}_2$  ( $\text{Li}_x\text{NCM271}$ ) and  $\text{Li}_x\text{Ni}_{0.9}\text{Co}_{0.05}\text{Mn}_{0.05}\text{O}_2$  ( $\text{Li}_x\text{NCM955}$ ) structure (space group:  $R\bar{3}m$ ) using a  $2 \times 2 \times 1$  and  $4 \times 4 \times 1$  unit cell, respectively. To perform DFT calculations gamma-centred  $k$ -point meshes of  $4 \times 4 \times 1$  and  $2 \times 2 \times 2$  were applied for  $\text{Li}_x\text{NCM271}$  and  $\text{Li}_x\text{NCM955}$  structures respectively. An energy cut off of 800 eV as well as electronic and force convergence criteria of  $10^{-5}$  eV and  $10^{-3}$  eV  $\text{\AA}^{-1}$ , respectively, were considered. For the calculation of elastic constants  $C_{ij}$ , we kept fixed the magnetic moment and atomic coordinates to the optimised ones for the equilibrium lattice parameters.  $C_{ij}$  matrix was computed using the strain values of 0,  $\pm 0.5\%$ , and  $\pm 1\%$ . After computing  $C_{ij}$ , we obtained the mechanical properties such as Young's, bulk and shear modulus as well as Poisson's ratio by using the Voigt–Reuss–Hill (VRH) homogenisation scheme.<sup>32</sup> To find the position of TM (Ni, Co, and Mn) and Li ions in  $\text{Li}_{1.0}\text{NCM271}$  (modelled by  $\text{Li}_{12}\text{Ni}_2\text{Co}_9\text{Mn}_1\text{O}_{24}$ ) and  $\text{Li}_{1.0}\text{NCM955}$  (modelled by  $\text{Li}_{48}\text{Ni}_{44}\text{Co}_2\text{Mn}_2\text{O}_{96}$ ) we first modelled and calculated the Coulomb energy ( $E_C$ ) of all possible structures and then performed DFT on minimum energy ones. Total Coulomb energy calculations were carried out using the so-called supercell code.<sup>33</sup>

**$\text{Li}_x\text{Ni}_{0.2}\text{Co}_{0.7}\text{Mn}_{0.1}\text{O}_2$  ( $\text{Li}_x\text{NCM271}$ ).** We computed  $E_C$  for  $\frac{12!}{2!10!} \times \frac{10!}{1!9!} = 660$  possible structures with 1 Mn, 2Ni, and 9 Co ions in 12 TM sites to find the position of TM ions in  $\text{Li}_{1.0}\text{Ni}_{0.2}\text{Co}_{0.7}\text{Mn}_{0.1}\text{O}_2$ . Afterwards, we kept fixed the position of TM ions in the determined lowest  $E_C$  structure among 660 configurations and obtained the position of Li ions for  $\text{Li}_{0.5}\text{Ni}_{0.2}\text{Co}_{0.7}\text{Mn}_{0.1}\text{O}_2$  by calculating  $E_C$  for  $\frac{12!}{6!6!} = 924$  structures with 6 Li ions in 12 Li sites. The following charges were considered for Li, TM (Ni, Co and Mn), and O ions, respectively:  $1^+$ ,  $3^+$  ( $3.5^+$  for half delithiation), and  $2^-$ . Finally, by performing DFT-PBE calculation on 5 distinguishable topmost favourable structures from electrostatic analysis on  $\text{Li}_{0.5}\text{Ni}_{0.2}\text{Co}_{0.7}\text{Mn}_{0.1}\text{O}_2$  we obtained the lowest total energy structure.

**$\text{Li}_x\text{Ni}_{0.9}\text{Co}_{0.05}\text{Mn}_{0.05}\text{O}_2$  ( $\text{Li}_x\text{NCM955}$ ).** We computed  $E_C$  for  $\frac{48!}{2!46!} \times \frac{46!}{2!44!} = 1.17 \times 10^6$  structures with 2 Mn, 2 Co and 44 Ni ions in 48 TM sites to find the position of TM ions in  $\text{Li}_{1.0}\text{Ni}_{0.9}\text{Co}_{0.05}\text{Mn}_{0.05}\text{O}_2$ . Then, we carried out DFT-PBE calculations on 2 configurations with lowest energies: (i) Mn and Co at the same layer and (ii) Mn and Co at different layers. The second configuration was found to be more favourable. Finding

position of Li ions in  $\text{Li}_{0.5}\text{Ni}_{0.9}\text{Co}_{0.05}\text{Mn}_{0.05}\text{O}_2$  is (computationally) a formidable task due to the large number of possible configurations with 24 Li ions in 48 Li sites. For this reason, we considered the arrangement of Li ions in  $\text{Li}_{0.5}\text{Ni}_{0.2}\text{Co}_{0.7}\text{Mn}_{0.1}\text{O}_2$  for  $\text{Li}_{0.5}\text{Ni}_{0.9}\text{Co}_{0.05}\text{Mn}_{0.05}\text{O}_2$ .

### Material parameters

The maximum strain over the course of delithiation is crucial for the effect of mechanical fatigue. This occurs in all considered cathode active materials approximately at the point of half lithiation ( $x = 0.5$ ), except for NCM955. For this material the largest strains are found for higher states of charge ( $x < 0.5$ ), we selected  $x = 0.1$ . Notwithstanding, the largest difference in the anisotropic lattice strains is observed for  $x = 0.5$  also for NMC955. As has been shown, depending on the electrolyte stiffness, one or the other state of charge leads to the maximum stress. Hence, both cases have been considered and the results with the maximum stress are given in the main article and the other case in the ESI.†

The stiffness matrices for the anisotropic materials and the Young's moduli and Poisson ratios for the isotropic materials are summarised together with chemical strains of the cathode active materials in Table 2. As no values for LATP were available, the calculated values for the similar  $\text{LiTi}_2(\text{PO}_4)_3$  have been used.

### Simulation setup and boundary conditions

The charging rate was assumed to be low enough that the resulting Li concentration gradients inside the cathode were negligible. This is typically the case for C rates not larger than 0.1 (sometimes 1, for low CAM content and small grain sizes). Thus, comparable benchmark stresses are calculated emerging in a perfectly working battery (no isolated CAM regions are present).

The constitutive equation of the linear elastic chemo-mechanical calculations are given in the ESI, p. S1–S2.† We calculated the stresses of composite cathodes of different compositions at these given state of charge (Table 2) and compared the different material combinations. According to the Pugh criterion, the materials with the given elastic constants do not express a significant ductility, but were assumed to behave elastically until fracture. The fracture process itself was not part of the model. Until now, there are no strength data available to conclude the exact point of failure. Still, the analyses of the resulting stresses can serve as a guideline for lowering mechanical stresses in composite cathodes of all-solid-state batteries avoiding stress concentrations detrimental to the fracture strength of the composite. Furthermore, a reliable battery should not show crack formation at all, but exhibit low stresses; the material combination which show these can be found with our screening approach. Since we study the effect of the mere delithiation in this work, no thermal mismatch stresses of the manufacturing processes were taken into account. These thermo-elastic stresses arising during cooling from the sintering temperature to room temperature simply add to the electrochemically induced stresses.



**Table 2** Elastic parameters (anisotropic stiffness matrix  $C$ , Young's modulus  $E$ , Poisson ratio  $\nu$ , and bulk modulus  $B$ ) and chemical strains for different cathode active materials and electrolyte materials. Values without references were calculated with DFT. VHR values denote the Voigt–Reuss–Hill approximation from the stiffness matrix<sup>34–37</sup>

Elastic parameters	Chemical strains
<p><b>Li<sub>0.5</sub>NCM271</b></p> $C = \begin{pmatrix} 242.2 & 87.4 & 136.0 & 0 & 0 & 0 \\ & 242.2 & 136.0 & 0 & 0 & 0 \\ & & 188.0 & 0 & 0 & 0 \\ & \text{sym.} & & 146.2 & 0 & 0 \\ & & & & 146.2 & 0 \\ & & & & & 77.4 \end{pmatrix} \text{ GPa}$ <p>(<math>E_{\text{VHR}} = 221</math> GPa, <math>\nu_{\text{VHR}} = 0.26</math>, <math>B_{\text{VHR}} = 155</math> GPa)</p>	<p><math>\epsilon_a = -0.83\%</math>,  <math>\epsilon_c = +0.79\%</math>  (ref. 11)</p>
<p><b>Li<sub>0.5</sub>NCM361</b>  Same as Li<sub>0.5</sub>NCM271</p>	<p><math>\epsilon_a = -1.08\%</math>,  <math>\epsilon_c = +1.26\%</math>  (ref. 11)</p>
<p><b>Li<sub>0.5</sub>NCM955</b></p> $C = \begin{pmatrix} 279.1 & 117.8 & 107.7 & 0 & 0 & 0 \\ & 279.1 & 107.7 & 0 & 0 & 0 \\ & & 184.6 & 0 & 0 & 0 \\ & \text{sym.} & & 75.2 & 0 & 0 \\ & & & & 75.2 & 0 \\ & & & & & 80.6 \end{pmatrix} \text{ GPa}$ <p>(<math>E_{\text{VHR}} = 195</math> GPa, <math>\nu_{\text{VHR}} = 0.29</math>, <math>B_{\text{VHR}} = 153</math> GPa)</p>	<p><math>\epsilon_a = -1.23\%</math>,  <math>\epsilon_c = +2.81\%</math></p>
<p><b>Li<sub>0.1</sub>NCM955</b></p> $C = \begin{pmatrix} 278.0 & 91.5 & 114.2 & 0 & 0 & 0 \\ & 278.0 & 114.2 & 0 & 0 & 0 \\ & & 158.7 & 0 & 0 & 0 \\ & \text{sym.} & & 70.6 & 0 & 0 \\ & & & & 70.6 & 0 \\ & & & & & 93.2 \end{pmatrix} \text{ GPa}$ <p>(<math>E_{\text{VHR}} = 188</math> GPa, <math>\nu_{\text{VHR}} = 0.29</math>, <math>B_{\text{VHR}} = 146</math> GPa)</p>	<p><math>\epsilon_a = -3.95\%</math>,  <math>\epsilon_c = -3.09\%</math></p>
<p><b>Li<sub>0.5</sub>CoO<sub>2</sub></b></p> $C = \begin{pmatrix} 308.6 & 78.3 & 84.9 & 0 & 0 & 0 \\ & 308.6 & 84.9 & 0 & 0 & 0 \\ & & 187.9 & 0 & 0 & 0 \\ & \text{sym.} & & 64.1 & 0 & 0 \\ & & & & 64.1 & 0 \\ & & & & & 115.2 \end{pmatrix} \text{ GPa}$ <p>(<math>E_{\text{VHR}} = 212</math> GPa, <math>\nu_{\text{VHR}} = 0.25</math>, <math>B_{\text{VHR}} = 141</math> GPa)</p>	<p><math>\epsilon_a = -0.23\%</math>,  <math>\epsilon_c = +2.38\%</math>  (ref. 13, 38 and 39)</p>
<p><b>PEO</b>  <math>E = 0.1</math> GPa, <math>\nu = 0.4</math>, <math>B = 0.167</math> GPa</p>	<p><math>\epsilon = 0\%</math></p>

**Table 2** (Contd.)

Elastic parameters	Chemical strains
<p><b>LPS</b></p> $C = \begin{pmatrix} 32.1 & 10.9 & 19.7 & 0 & 0 & 0 \\ & 38.1 & 17.4 & 0 & 0 & 0 \\ & & 51.8 & 0 & 0 & 0 \\ & \text{sym.} & & 10.5 & 0 & 0 \\ & & & & 9.5 & 0 \\ & & & & & 13.7 \end{pmatrix} \text{ GPa}$ <p>(ref. 21)  (<math>E_{\text{VRH}} = 31.2</math> GPa, <math>\nu_{\text{VRH}} = 0.28</math>, <math>B_{\text{VHR}} = 23.3</math> GPa)</p>	<p><math>\epsilon = 0\%</math></p>
<p><b>LATP</b></p> $C = \begin{pmatrix} 226.0 & 86.7 & 43.9 & 7.9 & 0 & 0 \\ & 226.0 & 43.9 & -7.9 & 0 & 0 \\ & & 116.3 & 0 & 0 & 0 \\ & \text{sym.} & & 48.6 & 0 & 0 \\ & & & & 48.6 & 7.9 \\ & & & & & 69.6 \end{pmatrix} \text{ GPa}$ <p>value for LiTi<sub>2</sub>(PO<sub>4</sub>)<sub>3</sub> (ref. 21)  (<math>E_{\text{VRH}} = 146</math> GPa,  <math>\nu_{\text{VRH}} = 0.24</math>,  <math>B_{\text{VHR}} = 95.1</math> GPa)</p>	<p><math>\epsilon = 0\%</math></p>
<p><b>LLZO</b>  <math>E = 146</math> GPa, <math>\nu = 0.26</math>, <math>B = 101</math> GPa</p>	<p><math>\epsilon = 0\%</math></p>

The 3D microstructure acquired by FIB-SEM and the computer-generated microstructures served as representative volume elements (RVE). Thus they represent a bulk cathode of infinite extent using symmetric (Dirichlet) boundary conditions in all directions. The composite cathode was considered as free-standing, hence no constraints were applied. The stress calculations were carried out using the ElastoDict FeelMath-LD module of the GeoDict software with a conjugate gradient voxel based solver.<sup>40,41</sup> The geometry was discretised with a regular voxel grid skipping the necessity of complex meshing required by finite element solvers. As all deformations were small the small deformation theory was used.

### Stress representation

Stress histograms served as the main type for stress representation in this work. They show the differential relative frequency as a function of the stress value. The differential relative frequency  $\tilde{n}_k$  was determined from the absolute frequency  $N_k$  of the stress  $S$  inside the stress interval  $[S_k, S_{k+1}]$  by:

$$\tilde{n}_k = \frac{N_k}{(S_{k+1} - S_k) \sum_j N_j}$$

which is independent from the interval size chosen. An interval size of  $S_{k+1} - S_k = 8$  MPa was used. In this work, the frequencies





for all three principal stresses were summed up to represent the overall stress state.

## Author contributions

Robert Mücke: conceptualisation, methodology, investigation, validation, visualisation, writing – original draft. Najma Yaqoob: investigation, writing – original draft. Martin Finsterbusch: writing – review & editing. Fadi Al-Jaljoui: methodology, investigation. Payam Kaghazchi: methodology, supervision, writing – review & editing. Dina Fattakhova-Rohlfing: funding acquisition, writing – review & editing. Olivier Guillon: conceptualisation, supervision, writing – review & editing.

## Conflicts of interest

There are no conflicts to declare.

## Acknowledgements

Financial support from the German Ministry of Education and Research (BMBF) under grant number 13XP0510A (CatSE2) and 13XP0434A (FestBatt 2 – Oxid) is gratefully acknowledged. P. K. acknowledges the computing time granted through JARA-HPC on the supercomputer JURECA at Forschungszentrum Jülich.

## References

- 1 A. O. Kondrakov, A. Schmidt, J. Xu, H. Gesswein, R. Monig, P. Hartmann, H. Sommer, T. Brezesinski and J. Janek, *J. Phys. Chem. C*, 2017, **121**, 3286–3294.
- 2 T. Li, X.-Z. Yuan, L. Zhang, D. Song, K. Shi and C. Bock, *Electrochem. Energy Rev.*, 2020, **3**, 43–80.
- 3 W. Hua, S. Wang, M. Knapp, S. J. Leake, A. Senyshyn, C. Richter, M. Yavuz, J. R. Binder, C. P. Grey, H. Ehrenberg, S. Indris and B. Schwarz, *Nat. Commun.*, 2019, **10**, 5365.
- 4 P. Teichert, G. G. Eshetu, H. Jahnke and E. Figgemeier, *Batteries*, 2020, **6**, 8.
- 5 L. de Biasi, A. O. Kondrakov, H. Gesswein, T. Brezesinski, P. Hartmann and J. Janek, *J. Phys. Chem. C*, 2017, **121**, 26163–26171.
- 6 J. P. Pender, G. Jha, D. H. Youn, J. M. Ziegler, I. Andoni, E. J. Choi, A. Heller, B. S. Dunn, P. S. Weiss, R. M. Penner and C. B. Mullins, *ACS Nano*, 2020, **14**, 1243–1295.
- 7 L. Mu, R. Lin, R. Xu, L. Han, S. Xia, D. Sokaras, J. D. Steiner, T.-C. Weng, D. Nordlund, M. M. Doeff, Y. Liu, K. Zhao, H. L. Xin and F. Lin, *Nano Lett.*, 2018, **18**, 3241–3249.
- 8 A. Mukhopadhyay and B. W. Sheldon, *Prog. Mater. Sci.*, 2014, **63**, 58–116.
- 9 Y. He, C. Lu, S. Liu, W. Zheng and J. Luo, *Adv. Energy Mater.*, 2019, **9**, 1901810.
- 10 A. Y. Hou, C. Y. Huang, C. L. Tsai, C. W. Huang, R. Schierholz, H. Y. Lo, H. Tempel, H. Kungl, R. A. Eichel, J. K. Chang and W. W. Wu, *Adv. Sci.*, 2022, **10**, 2205012.
- 11 F. Strauss, L. de Biasi, A. Y. Kim, J. Hertle, S. Schweidler, J. Janek, P. Hartmann and T. Brezesinski, *ACS Mater. Lett.*, 2020, **2**, 84–88.
- 12 Y. Y. Ren, T. Danner, A. Moy, M. Finsterbusch, T. Hamann, J. Dippell, T. Fuchs, M. Muller, R. Hoft, A. Weber, L. A. Curtiss, P. Zapol, M. Klenk, A. T. Ngo, P. Barai, B. C. Wood, R. P. Shi, L. W. F. Wan, T. W. Heo, M. Engels, J. Nanda, F. H. Richter, A. Latz, V. Srinivasan, J. Janek, J. Sakamoto, E. D. Wachsman and D. Fattakhova-Rohlfing, *Adv. Energy Mater.*, 2022, **13**, 2201939.
- 13 R. Mücke, M. Finsterbusch, P. Kaghazchi, D. Fatakowa-Rohlfing and O. Guillon, *J. Power Sources*, 2021, **489**, 229430.
- 14 V. Malave, J. R. Berger, H. Y. Zhu and R. J. Kee, *Electrochim. Acta*, 2014, **130**, 707–717.
- 15 L. Wu, X. Xiao, Y. Wen and J. Zhang, *J. Power Sources*, 2016, **336**, 8–18.
- 16 H. Mendoza, S. A. Roberts, V. E. Brunini and A. M. Grillet, *Electrochim. Acta*, 2016, **190**, 1–15.
- 17 L. J. Miara, W. D. Richards, Y. E. Wang and G. Ceder, *Chem. Mater.*, 2015, **27**, 4040–4047.
- 18 F. D. Han, Y. Z. Zhu, X. F. He, Y. F. Mo and C. S. Wang, *Adv. Energy Mater.*, 2016, **6**, 1501590.
- 19 W. D. Richards, L. J. Miara, Y. Wang, J. C. Kim and G. Ceder, *Chem. Mater.*, 2016, **28**, 266–273.
- 20 Y. G. Lee, S. Fujiki, C. Jung, N. Suzuki, N. Yashiro, R. Omoda, D. S. Ko, T. Shiratsuchi, T. Sugimoto, S. Ryu, J. H. Ku, T. Watanabe, Y. Park, Y. Aihara, D. Im and I. T. Han, *Nat. Energy*, 2020, **5**, 299–308.
- 21 Z. Deng, Z. B. Wang, I. H. Chu, J. Luo and S. P. Ong, *J. Electrochem. Soc.*, 2016, **163**, A67–A74.
- 22 Y. H. Zhang, F. Chen, D. J. Yang, W. P. Zha, J. Y. Li, Q. Shen, X. L. Zhang and L. M. Zhang, *J. Electrochem. Soc.*, 2017, **164**, A1695–A1702.
- 23 F. Al-Jaljoui, R. Mücke, P. Kaghazchi, Y. J. Sohn, M. Finsterbusch, D. Fattakhova-Rohlfing and O. Guillon, *J. Energy Storage*, 2023, **68**, 107784.
- 24 M. Ihrig, L.-Y. Kuo, S. Lobe, A. M. Laptev, C.-a. Lin, C.-h. Tu, R. Ye, P. Kaghazchi, L. Cressa, S. Eswara, S.-k. Lin, O. Guillon, D. Fattakhova-Rohlfing and M. Finsterbusch, *ACS Appl. Mater. Interfaces*, 2023, **15**, 4101–4112.
- 25 W. S. Scheld, S. Lobe, C. Dellen, M. Ihrig, G. Häuschen, L. C. Hoff, M. Finsterbusch, S. Uhlenbruck, O. Guillon and D. Fattakhova-Rohlfing, *J. Power Sources*, 2022, **545**, 231872.
- 26 M. Rosen, M. Finsterbusch, O. Guillon and D. Fattakhova-Rohlfing, *J. Mater. Chem. A*, 2022, **10**, 2320–2326.
- 27 R. Ye, M. Ihrig, E. Figgemeier, D. Fattakhova-Rohlfing and M. Finsterbusch, *ACS Sustainable Chem. Eng.*, 2023, **11**, 5184–5194.
- 28 C. Roitzheim, Y. J. Sohn, L.-Y. Kuo, G. Häuschen, M. Mann, D. Sebold, M. Finsterbusch, P. Kaghazchi, O. Guillon and D. Fattakhova-Rohlfing, *ACS Appl. Energy Mater.*, 2022, **5**, 6913–6926.
- 29 P. E. Blöchl, *Phys. Rev. B: Condens. Matter Mater. Phys.*, 1994, **50**, 17953–17979.
- 30 G. Kresse and J. Furthmüller, *Phys. Rev. B: Condens. Matter Mater. Phys.*, 1996, **54**, 11169–11186.



- 31 J. P. Perdew, K. Burke and M. Ernzerhof, *Phys. Rev. Lett.*, 1996, **77**, 3865–3868.
- 32 D. H. Chung and W. R. Buessem, *J. Appl. Phys.*, 1967, **38**, 2010–2012.
- 33 K. Okhotnikov, T. Charpentier and S. Cadars, *J. Cheminf.*, 2016, **8**, 17.
- 34 W. Voigt, *Lehrbuch der Kristallphysik (mit Ausschluß der Kristalloptik)*, B. G. Teubner, Leipzig, Berlin, 1910.
- 35 A. Reuss, *J. Appl. Math. Mech.*, 1929, **9**, 49–58.
- 36 R. Hill, *Proc. Phys. Soc., Sect. A*, 1952, **65**, 349–354.
- 37 O. L. Anderson, *J. Phys. Chem. Solids*, 1963, **24**, 909–917.
- 38 X. Wang, I. Loa, K. Kune, K. Syassen and M. Amboage, *Phys. Rev. B: Condens. Matter Mater. Phys.*, 2005, **72**, 224102.
- 39 Y. Takahashi, N. Kijima, K. Dokko, M. Nishizawa, I. Uchida and J. Akimoto, *J. Solid State Chem.*, 2007, **180**, 313–321.
- 40 H. Moulinec and P. Suquet, *Comput. Methods Appl. Mech. Eng.*, 1998, **157**, 69–94.
- 41 M. Schneider, F. Ospald and M. Kabel, *Int. J. Numer. Methods Eng.*, 2016, **105**, 693–720.

